Electromechanical Considerations in Developing Low-Voltage RF MEMS Switches

Dimitrios Peroulis, *Member, IEEE*, Sergio P. Pacheco, *Member, IEEE*, Kamal Sarabandi, *Fellow, IEEE*, and
Linda P. B. Katehi, *Fellow, IEEE*

***Abstract*—This paper reports on the design, fabrication, and testing of a low-actuation voltage Microelectromechanical systems (MEMS) switch for high-frequency applications. The mechanical design of low spring-constant folded-suspension beams is presented first, and switches using these beams are demonstrated with measured actuation voltages of as low as 6 V. Furthermore, common nonidealities such as residual in-plane and gradient stress, as well as down-state stiction problems are addressed, and possible solutions are discussed. Finally, both experimental and theoretical data for the dynamic behavior of these devices are presented. The results of this paper clearly underline the need of an integrated design approach for the development of ultra low-voltage RF MEMS switches.**

***Index Terms*—Low actuation voltage, microelectromechanical systems (MEMS) switches, residual stress, spring constant, switching speed, top-electrode switches.**

I. INTRODUCTION

MICROMACHINING and microelectromechanical systems (MEMS) are among the most promising enabling technologies for developing low-power low-cost miniaturized RF components for high-frequency applications. Several universities and companies have developed RF MEMS switches [1]–[8] in the last decade that can be primarily classified as: 1) series or shunt; 2) fixed–fixed membranes or cantilever beams; and 3) capacitive or metal-to-metal contact type [9]. The main driving force behind this major research effort is the outstanding demonstrated RF performance of the MEMS switches from dc to 100 GHz compared to p-i-n diodes or FET transistors. Furthermore, electrostatically driven switches require only a few microwatts of dc power compared to several milliwatts that their solid-state counterparts dissipate. It is for this reason, as well as for the simplicity of their biasing networks, that most of the developed switches are electrostatic in nature.

These studies, however, have only limited their focus on the RF performance of MEMS switches and have provided little information on several important phenomena directly related to the inherent electromechanical characteristics of these structures. Their sheer interdisciplinary nature imposes a very tight coupling between the electrical and mechanical domains. For instance, thin-film residual stress and viscous damping may have a far greater influence on the performance of the device than intuitively anticipated. Moreover, the vast majority of the switches in the literature typically require a pull-in and hold-down voltage of 40–100 and 15–30 V, respectively. Whereas no difficulty exists in achieving these ranges in a typical laboratory environment, they may be quite challenging for handheld mobile phones, automotive vehicles, and similar wireless devices that rely on low-voltage power supplies. In addition, Goldsmith *et al.* [16] have shown that the lifetime of capacitive switches strongly depends on the applied actuation voltage. In particular, for capacitance switches, they experimentally observed a lifetime improvement of a decade for every 5–7-V drop on the switch pull-in voltage. Consequently, reducing the actuation voltage of MEMS switches may not only broaden the range of their possible applications, but also significantly enhance their performance. It would seem, therefore, that further investigations are needed in order to provide the MEMS engineer with complete and accurate information on the design and operation of these devices.

It is the purpose of this paper to present the results of our investigation on these issues. First, in Section II, we focus on the design of the low spring-constant beams that support the main switch structure. We also demonstrate a number of designs that resulted in switches with pull-in voltages of as low as 6 V. Section III discusses the effects of residual axial and gradient stress on the device performance and shows how minor design and fabrication details may have a significant impact on the final structure. Section IV concludes our study by presenting experimental and theoretical results on the dynamic behavior of the low-voltage MEMS switch.

II. SPRING CONSTANT AND ACTUATION VOLTAGE

A. Design

The mechanical design of most electrostatically based switches starts with considering the required dc actuation voltage. Equation (1) presents a widely cited formula (e.g., [8])

Manuscript received April 22, 2002. This work was supported by the System on a Chip/Jet Propulsion Laboratory under the Center for Integrated Space Microsystems Project and by the Department of Defense Research and Engineering under the Multidisciplinary University Research Initiative on “Low Power Electronics” and “Multifunctional Adaptive Radio, Radar and Sensors” programs.

D. Peroulis and K. Sarabandi are with the Radiation Laboratory, Electrical Engineering and Computer Science Department, The University of Michigan at Ann Arbor, Ann Arbor, MI 48109-2122 USA (e-mail: dperouli@engin.umich.edu).

S. P. Pacheco was with the Radiation Laboratory, Electrical Engineering and Computer Science Department, The University of Michigan at Ann Arbor, Ann Arbor, MI 48109-2122 USA. He is now with Digital DNA Laboratories, Motorola, Tempe, AZ 85284 USA.

L. P. B. Katehi was with the Radiation Laboratory, Electrical Engineering and Computer Science Department, The University of Michigan at Ann Arbor, Ann Arbor, MI 48109-2122 USA. She is now with the College of Engineering, Purdue University, West Lafayette, IN 47907 USA.

Digital Object Identifier 10.1109/TMTT.2002.806514

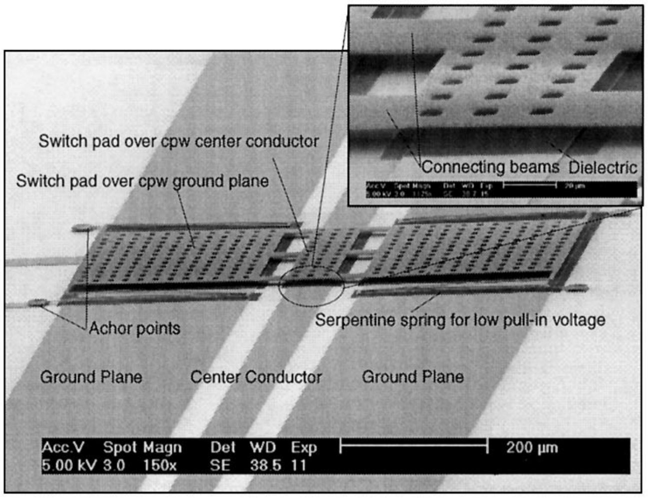

Fig. 1. SEM picture of the proposed low-voltage capacitive shunt switch over a CPW line.

for calculating the pull-in voltage of fixed-fixed beams or air bridges as follows:

$$V_p = \sqrt{\frac{8K_z g_0^3}{27\epsilon_0 A}}. \tag{1}$$

K_z is the equivalent spring constant of the moving structure in the direction of desired motion (typically the z-direction), g_0 is the gap between the switch and the actuation electrode, ϵ_0 is the free-space permittivity, and A is the switch area where the electrostatic force is applied. Equation (1) implies that there are several ways that may decrease the required actuation voltage. For instance, reducing g_0 can significantly lower the pull-in voltage. Although this solution can be partly applied to low-frequency applications ($<$10 GHz), it will adversely affect the high-frequency off-state switch performance by compromising the switch isolation (for a series switch) or insertion loss (for a shunt switch). A second approach in lowering the pull-in voltage would be to increase the actuation area A. This area, however, has to stay within reasonable limits, primarily imposed by our desire for miniaturized circuits. The third alternative, which offers the maximum design flexibility for a low-to-moderate actuation voltage, is to lower the switch spring constant, hence, designing a compliant switch.

Fig. 1 shows an SEM picture of our proposed switch in a coplanar waveguide (CPW) configuration. The switch consists of three movable metallic plates, one over each conductor of the CPW line. These plates are connected together with three short beams (connecting beams) and the whole structure is connected to the substrate at four points (anchors) through four beams. Due to their shape, we will call these beams serpentine springs or folded-suspension beams. The switch is typically suspended 3–4 μm above the CPW line and is electrostatically actuated when a dc voltage is applied between the switch and the CPW ground planes.

B. Fabrication

The fabrication process is fairly simple, requires only four masks, and is described in detail in [10]. The CPW line is typically made of Ti/Au (500/9000 Å) and is defined first through a liftoff process. A plasma-enhanced chemical vapor deposition (PECVD) of approximately 1400–2000 Å Si_3N_4 follows. Since the switch is made of metal (typically Ni), this dielectric layer is primarily needed during the actuation stage to prevent a direct dc contact between the switch and CPW line. Therefore, a positive photoresist intended to protect the Si_3N_4 underneath the switch is deposited with a normal lithography and the remaining dielectric layer is etched through a reactive ion etching (RIE) process. After the photoresist removal, the sacrificial layer (polyimide or photoresist) is deposited and the switch anchor points are photolithographically defined. Afterwards, a seed layer (typically Ti/Ni 2000/500 Å), is deposited, patterned, and electroplated. The last step is the removal of the sacrificial layer and the supercritical CO_2 drying of the structure.

C. Spring Design

Since the mathematical details of the electrostatic actuation [including (1)] have been extensively analyzed in the past [17], [18], we will just briefly describe the basic principle here. When no dc bias is applied, the switch presents a very small shunt capacitance (typically in the order of 30–50 fF) between the center conductor and ground planes. This is called the up or off state and the RF signal can propagate with minimal loss (typically with -0.1 dB at X-band). On the other hand, if the applied bias exceeds the actuation voltage, the switch collapses on the dielectric layer underneath, resulting in a significant shunt capacitance, which is equivalent to an RF short circuit. This is called the down or on state and virtually all the incident RF power is reflected back to the source.

As was previously mentioned, the switch of Fig. 1 is connected to the substrate through four serpentine springs that are used to substantially lower the switch spring constant. If k_z is the z-directed spring constant for each one of the springs, the total switch spring constant K_z is given by

$$K_z = 4k_z. \tag{2}$$

Compared to simple cantilever beams of equal total length, these springs have the additional advantage of occupying considerable less space, but they also show higher spring constant. As will be shown, however, adding more meanders can significantly lower it without excessively increasing the required space. In the following, we calculate the spring constant of an N-section meander [see Fig. 2(a)] when a virtual force F_z is applied at its free end. An analytical solution for a similar folded meander has been obtained by Fedder [19] and our analysis is based on his study.

Each meander of the whole spring is defined as the set of four beams: two primary beams of length a and two secondary beams of length b. Therefore, an N-meander spring has $2N$ primary beams and $2N$ secondary beams. The switch shown in Fig. 1, for instance, has a single-section meander ($N = 1$) with $a = 20$ μm and $b = 240$ μm. All the necessary dimensions and material constants for our switch are given in Table I. For the analytical calculation, it is assumed that all six degrees of freedom of the anchor point [point A in Fig. 2(a)] are fixed. Moreover, the guided-end boundary conditions are applied for the free-end

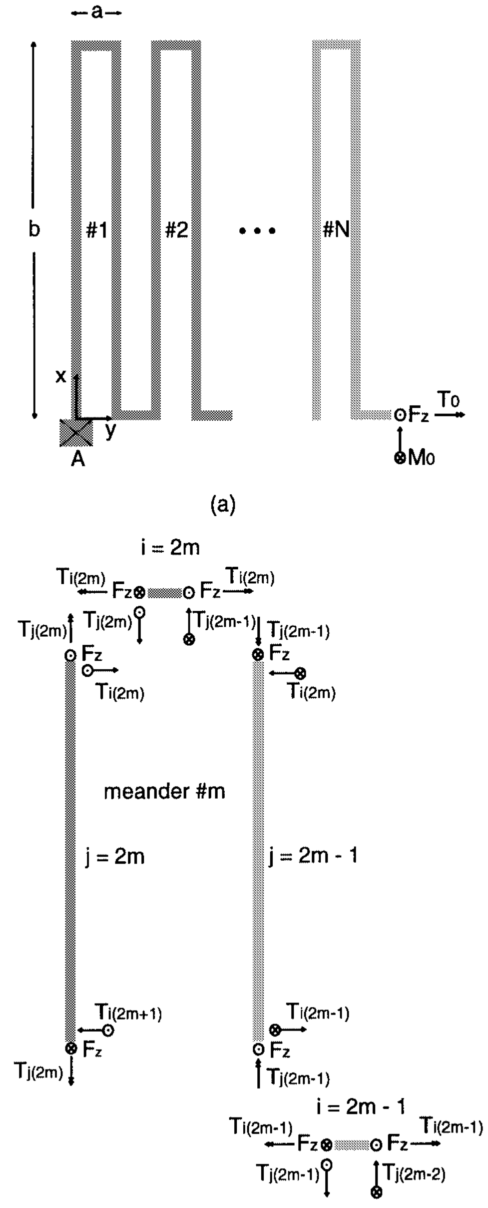

(a)

(b)

Fig. 2. (a) Schematic (drawn to scale) of an N-meander serpentine spring. (b) Forces, torques, and moments in the mth meander.

point of the spring since this point is attached to the main switch body. Consequently, a moment M_0 and a torsion T_0 are applied to this point to constrain the rotation angles around the x- and y-axes. The torsion and moment of each beam are then given by [19] [see Fig. 2(b)]

$$\begin{aligned}M_{a,i} &= M_0 - F_z\big[x+(i-1)\big]\\ T_{a,i} &= T_0 + \left[\frac{1+(-1)^i}{2}\right]F_z b\\ M_{b,j} &= (-1)^j T_0 - F_z x + \left[\frac{1+(-1)^j}{2}\right]F_z b\\ T_{b,j} &= (-1)^j\,(iF_z a - M_0)\end{aligned} \tag{3}$$

TABLE I

PHYSICAL DIMENSIONS AND MATERIAL CONSTANTS FOR THE LOW-VOLTAGE SWITCH

Primary meander length (a)	20 μm
Secondary meander length (b)	240 μm
Switch thickness (t)	2 μm
Beam width (both beams) (w)	5 μm
Ni Young's modulus (E)	207 GPa
Ni Poisson's ratio (ν)	0.31
Shear modulus (G)	$E/(2(1+\nu))$
x-axis moment of inertia (I_x)	$wt^3/12$
z-axis moment of inertia (I_z)	$tw^3/12$
polar moment of inertia (I_p)	$I_x + I_z$
Torsion constant (J)	$0.413I_p$ (see [20])

where $M_{a,i}$ and $T_{a,i}$ ($M_{b,j}$ and $T_{b,j}$) are the moment and torsion of the ith primary beam (jth secondary beam) with $i = 1$ to $2N$ ($j = 1$ to $2N$). In these equations, x is the longitudinal dimension along each one of the beams.

Following the virtual work method, the total elastic strain energy of the meander is given by

$$U = \sum_{i=1}^{2N}\int_0^a\left(\frac{M_{a,i}^2}{2EI_x}+\frac{T_{a,i}^2}{2GJ}\right)dx + \sum_{j=1}^{2N}\int_0^b\left(\frac{M_{b,j}^2}{2EI_x}+\frac{T_{b,j}^2}{2GJ}\right)dx \tag{4}$$

where I_x, I_z, G, and J are defined in Table I. Finally, the spring constant is given by

$$k_z = F_z\delta_z = F_z\frac{\partial U}{\partial F_z} \tag{5}$$

along with the boundary conditions

$$\phi_0 \equiv \frac{\partial U}{\partial M_0} = 0 \text{ and } \psi_0 \equiv \frac{\partial U}{\partial T_0} = 0. \tag{6}$$

These equations lead to the following expressions for the reactions M_0 and T_0:

$$M_0 = \frac{\dfrac{2Na}{EI_x}+\dfrac{(2N+1)b}{GJ}}{2\left(\dfrac{a}{EI_x}+\dfrac{b}{GJ}\right)}aF_z \tag{7}$$

$$T_0 = -\frac{F_z b}{2} \tag{8}$$

and for the spring constant k_z

$$k_z = \left[\frac{8N^3a^3+2Nb^3}{3EI_x}+\frac{abN\big[3b+(2N+1)(4N+1)a\big]}{3GJ} - \frac{Na^2\left[\dfrac{2Na}{EI_x}+\dfrac{(2N+1)b}{GJ}\right]^2}{2\left(\dfrac{a}{EI_x}+\dfrac{b}{GJ}\right)} - \frac{Nb^2}{2}\left(\frac{a}{GJ}+\frac{b}{EI_x}\right)\right]^{-1}. \tag{9}$$

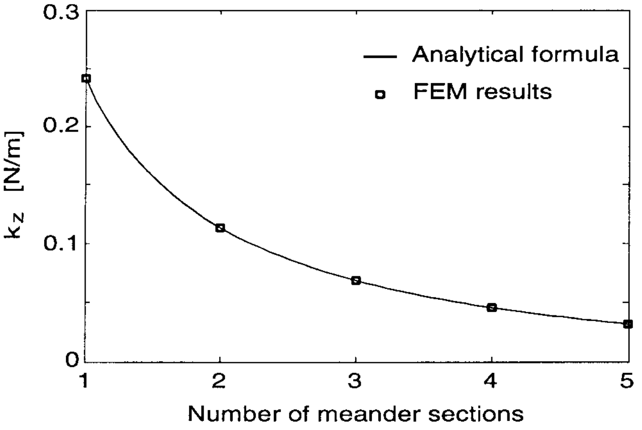

Fig. 3. Analytically computed and FEM simulated results of the z-directed spring constant of an N-section meander.

Although (9) is lengthy, it is written in an intuitive way that may facilitate the design of these meanders or similar beams. The first two terms of the denominator represent the percentage of the spring constant that is due to beam bending (first term) and twisting (second term). In other words, these terms depend solely on the meander geometry and the ability of the beam material to bend and twist. The last two terms of the denominator are due to the boundary conditions of the meander moving end and correspond to its inability to rotate around the x- and y-axes. These two terms may have comparable magnitude to the first two and considerably increase the switch spring constant.

Equation (9) was verified by a commercially available finite-element method (FEM) code [21]. The dimensions of Table I were input in the code and several linear simulations were performed for springs with 1–5 meanders. For each simulation, a concentrated z-directed force of $F_z^{\mathrm{FEM}} = 1\ \mu\mathrm{N}$ was applied at the tip of the spring along with the necessary guided-end boundary conditions. The resulting deflection Δ_z was then computed and the FEM spring constant was extracted as $k_{mz}^{\mathrm{FEM}} = F_z^{\mathrm{FEM}}/\Delta_z$. Excellent agreement between the analytically and numerically computed spring constants is observed in Fig. 3, which graphically presents the two spring constants as a function of the number of the meanders. This graph also illustrates that the serpentine spring constant is not significantly reduced after including four or five meander sections. Hence, three or four meanders would be a good compromise between low spring-constant requirements and space limitations.

TABLE II
ACTUATION VOLTAGE MEASUREMENTS FOR SEVERAL MEMS SWITCHES

Meanders	Experimental		Theoretical	
	V_p [V]	K_z [N/m]	V_p [V]	K_z [N/m]
1	30	26.9	8.3	2.08
2	22	14.5	5.7	0.97
3	17	8.6	4.4	0.58
4	11	3.6	3.6	0.38
5	6	1.1	3.0	0.27

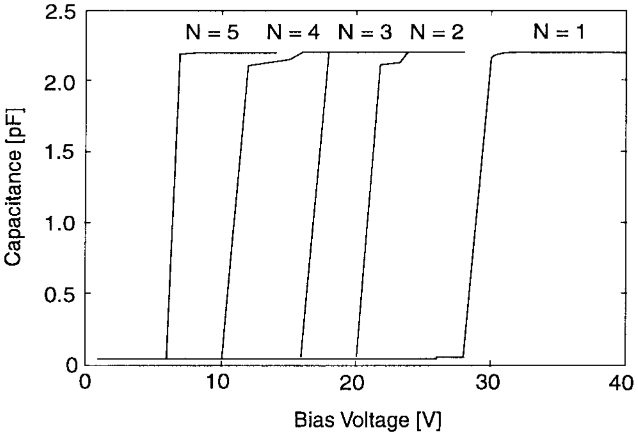

Fig. 4. Measured dc switch capacitance as a function of the applied bias voltage and number of meanders.

D. Actuation Voltage Measurements

Five switch designs with 1–5 meanders in their folded suspensions were fabricated and measured. Except for the serpentine springs, all designs were identical and were fabricated on the same wafer by the same fabrication process. For each design, we measured the pull-in voltage using an HP 4275A multifrequency LCR meter with an internal bias option. These measurements are presented in Table II, which also compares the extracted switch spring constant from the measured pull-in voltage [based on (1)] with the corresponding theoretical results. The theoretical values have been calculated for a switch thickness of $t = 2.5\ \mu\mathrm{m}$ (because of over-plating in the fabricated switches) and an initial gap of $g_0 = 5\ \mu\mathrm{m}$. The reason for this higher gap is that, although the sacrificial layer thickness was 4 μm, the induced residual stress across the structure caused a slight out-of-plane deflection, which, on average, increased the total distance from the substrate to 5 μm. We will discuss stress issues in more detail in Section III. Fig. 4 also shows the measured dc capacitance of the switches as a function of the applied bias voltage and the number of meanders.

These data reveal several discrepancies between the simulated and measured results. The first dissimilarity is the fact that the measured pull-in voltages are 5–10 times higher than the theoretically calculated ones. The second and most interesting one is related to the percentage of the spring-constant reduction as the number of meanders is increased. For example, when the number of meanders was increased from one to two, the experimentally extracted spring constant was decreased by 46%, while the theoretical calculations predicted 53%. Although these results are in fair agreement, this is not the case for switches with more meanders. The switches with five meanders, for instance, had 70% lower spring constant than the ones with four. According to (9), however, this number should be close to 30%. Fig. 5 graphically illustrates these observations for all cases. All these issues are due to the high intrinsic axial stress built into the Ni layer during the fabrication and are studied in Section III.

E. Stiction and Top Electrode Design

Although low spring constant is essential in obtaining low-voltage switches, preventing down-state stiction is equally

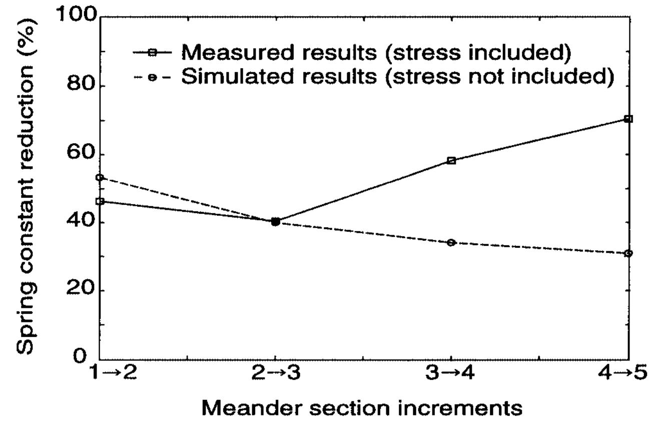

Fig. 5. Experimental and theoretical percentage change of the switch spring constant as the number of meanders is increased.

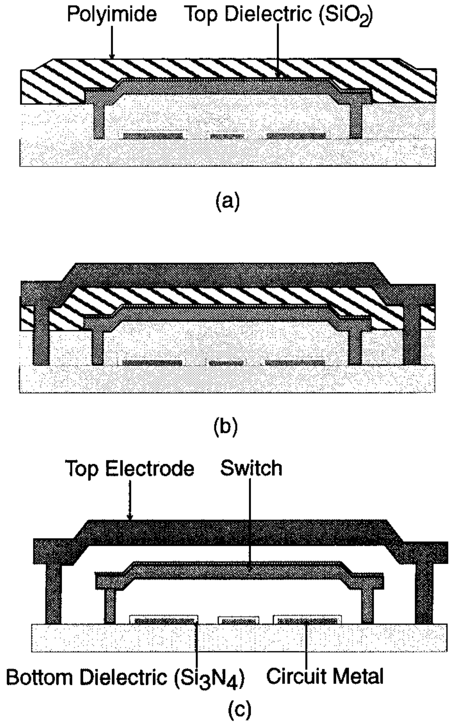

Fig. 6. Top electrode concept and fabrication process. (a) 2500 Å of SiO_2 are deposited on top of the switch followed by a second sacrificial layer. (b) The top electrode is electroplated in a low-stress Au solution. (c) The whole structure is released by etching the sacrificial layers followed by a standard supercritical drying process.

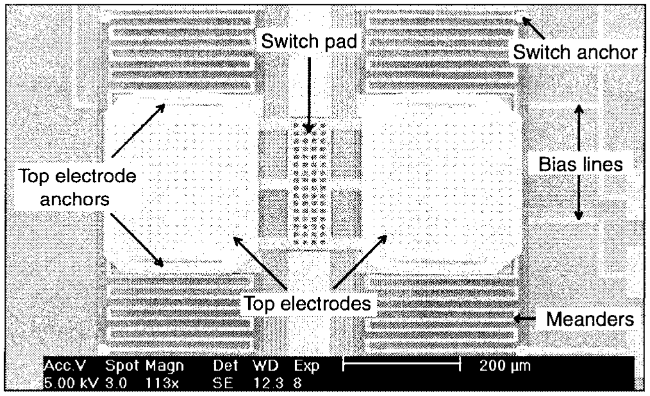

Fig. 7. Four-meander switch with top electrodes. Each top electrode is approximately 5–6-μm thick and is fabricated with a low-stress Au electroplated process.

important. A low-voltage switch experiences a relatively weak restoring force while in the down state, which may not be sufficiently high to pull the switch up, particularly in humid or contaminated environments. This drawback of this family of switches can be overcome by including top electrodes. Fig. 6 illustrates the idea of fabricating a metallic plate (top electrode) above the switch. By applying a dc voltage between this top electrode and switch, the switch can be pulled up from the down state, even if the restoring force is not sufficiently high.

Fig. 7 shows an example of a four-meander switch with top electrodes over the dc switch pads. There is no electrode suspended above the center conductor pad because such an electrode would significantly deteriorate the up-state switch capacitance. These top electrodes are very stiff fixed–fixed plates (5–6-μm-thick low-stress electroplated Au) with a spring constant higher than 2300 N/m. Any movement of these electrodes would require voltages in excess of 250 V and, compared with the switch, they can be considered as static plates. Additionally, they provide stabilization to the overall switch structure against severe mechanical shocks. Measured and theoretical results of switches with top electrodes and power measurements of the same switches are reported in [22].

III. INTRINSIC RESIDUAL STRESS ISSUES

Although the previous analysis allows for a first estimate of the switch spring constant and pull-in voltage, it does not account for any intrinsic residual stress on the structure. Residual stress, however, is developed during the fabrication of most microstructures and typically presents most of the major challenges in developing these devices. Under this stress, thin-film structures can experience undesirable deformations, which may be significant, particularly for high-aspect ratio structures. Additionally, many MEMS switches must satisfy very stringent requirements for reliable performance, including being planar over the circuit underneath it. Any undesirable buckling or curling may easily deteriorate the performance of the switch, or lead to the complete failure of the device. A lot of attention, therefore, has to be paid to residual stress and its effects on compliant structures before any successful devices can be developed.

When a thin film is deposited on a sacrificial layer at a temperature lower than its flow temperature, then intrinsic stresses develop in the film-sacrificial layer system [23]. A number of studies have been already performed to theoretically explain the mechanisms of these stresses [24], [25] and to experimentally measure their effects [26], [27]. Nonetheless, in general, thin-film stress is complicated and heavily depends on the specifics of the fabrication process. There is also very little information for metallic microstructures built by thin-films depositions and effective ways that can control its stress and/or its effects. This section illuminates the most important stress-related challenges for developing low-voltage switches.

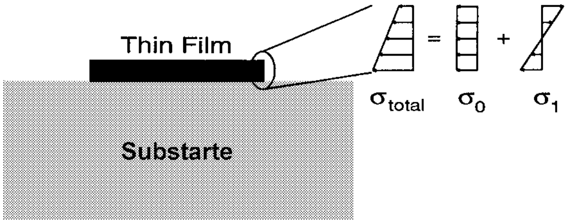

Fig. 8. Thin-film residual-stress approximation.

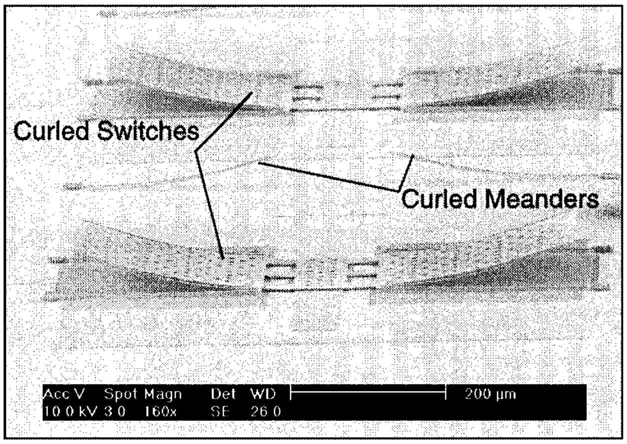

Fig. 9. Switches with considerable deflection as a result of a poorly designed fabrication process.

A. Gradient Residual Stress

A general uniaxial residual stress field in a thin film can be represented as [26]

$$\sigma_{\text{total}} = \sum_{k=0}^{\infty} \sigma_k \left(\frac{y}{\frac{h}{2}} \right)^k \tag{10}$$

where h is the film thickness and $y \in (-h/2, h/2)$ is the coordinate across the film thickness, with its origin at the mid-plane of the film. For a first-order approximation, the total stress can be calculated as

$$\sigma_{\text{total}} \simeq \sigma_0 + \sigma_1 \left(\frac{2y}{h} \right) \tag{11}$$

This equation implies that the total stress can be expressed as a superposition of the constant mean stress σ_0 (positive or negative depending on whether the film is in tension or compression) and a gradient stress σ_1 about the mid-plane (see Fig. 8). The effects of the gradient stress are analyzed in this subsection and those of the mean stress in the following one.

It is widely known that residual gradient stress causes undesirable out-of-plane deformation. Fig. 9 shows two examples of extremely warped switches. These switches were 4-μm thick and the maximum deformation, defined as the distance between the higher and lower switch points, was on average 30 μm. This deformation was recorded for switches 640-μm long (not counting the length of the meanders), but increased to 70–80 μm for switches close to 1-mm long. This substantial deformation renders both structures unusable because: 1) the required actuation voltage is much higher than the design value (>80 V) and 2) the up-state switch RF capacitance is considerably higher than anticipated ($C_{\text{up}} > 150$ fF, instead of 50 fF). The sacrificial and seed layers that resulted in such a stress were the polyimide DuPont PI2545 and an evaporated Ti/Ni (1500/500-Å) layer, respectively. The switches were then electroplated in an Ni solution (Nickel Sulfamate, Barrett SN by Mac Dermid) with a steady current density of 4 mA/cm^2 for approximately 30 min. The induced stress with this fabrication process was repeatable over a period longer than six months.

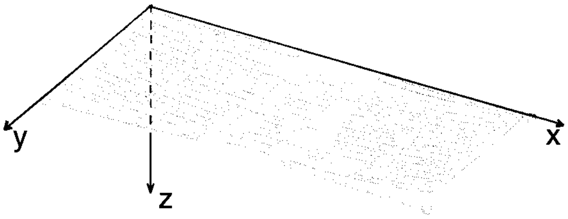

Fig. 10. Simulated warped switch structure (by SUGAR). The maximum switch deflection is approximately 23 μm.

This switch shape under residual gradient stress was also theoretically validated using SUGAR.[1] Fig. 10 shows the simulated switch shape, which agrees very well with the fabricated switches. The maximum gradient stress value in the software was varied until the measured maximum deflection was obtained.

One way to alleviate this problem without increasing the actuation voltage is to selectively increase the switch thickness [28]. In this technique, the main switch body thickness is increased to 6–8 μm, but the springs remain 2-μm thick [see Fig. 11(a)]. This process utilizes the following two electroplating steps:

Step 1) The switch and the springs are plated.
Step 2) The switch main body is subsequently plated again until it reaches a thickness of 6–8 μm.

Due to some adhesion difficulties between the two plated structures, the process was slightly changed by plating only a switch frame during the first step instead of the whole switch [see Fig. 11(b)]. This improvement resulted in a 98% yield.

The drawback of this technique, however, is that, although it limits the switch warping to 1–3 μm and may prove useful for other types of MEMS devices, it also results in less conformal switches with lower down-state capacitance than the original switches.

We experimentally found that a better solution is to sputter deposit the Ti layer (instead of evaporating) above the sacrificial layer. More specifically, the Ti sputtering process is performed with The University of Michigan at Ann Arbor sputtering tool with a dc source calibrated to deposit 90 Å/min under 7 mT of Ar pressure. The actual deposition is typically done for 25–26 min, resulting in a film of 2250–2350 Å of Ti. After the sputtering process is completed, the sample is immediately (in order to minimize Ti oxidation) taken to the Ni e-beam evaporator where 500 Å of Ni are deposited. It is also very important to point out that nothing else is changed in the process, including the Ni electroplating solution, current density, and sacrificial layer etching. Furthermore, this process can be followed with either polyimide or photoresist with negligible differences.

---

[1] [Online]. Available: http://www.bsac.eecs.berkeley.edu/cfm/

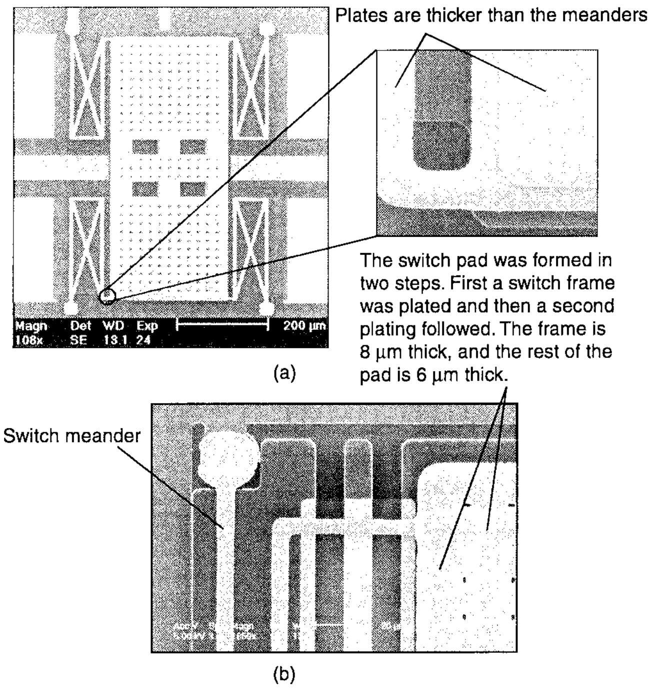

Fig. 11. Fabricated switches with the selective electroplating process. The adhesion problems of the first switch were solved by increasing the seed layer area that was exposed to the second plating.

Fig. 1 is one example of the plane switches fabricated with this process and Fig. 12 shows some details of three more examples. The switches shown in Figs. 1 and 12(a) are 2-μm thick and suspended over a 40/60/40-μm CPW line. Although the latter switch was fabricated with three meanders instead of one, no appreciable difference in the warping profile was observed. The maximum measured deflection (as defined in Fig. 9) for both of them is approximately 0.5 μm. This corresponds to less than 0.1% of the main switch length (640 μm) and does not affect the RF switch performance since it is strongly localized at the end of the dc actuation pad.

The improved fabrication process was also tested with switches only 1-μm thick, 680-μm long, and 240-μm wide. Two of these switches are shown in Fig. 12(b) and (c). Both switches include one meander, but in the first one, we have replaced the straight connecting beams with a second meandering beam. Evidently both structures are fairly plane and their residual gradient stress is nearly negligible. The first one, however, exhibits somewhat straighter profile, which is related to the axial residual stress, analyzed in the following section. This meandering connecting beam was originally employed to increase the shunt switch inductance [11], but it also proved useful in releasing the in-plane switch stress. As for the three short connecting beams, the slightly less plane switch may not appear very appealing at first, but it is very useful in limiting the high-frequency up-state insertion loss because it substantially reduces the up-state capacitance (by 50%–70%). Furthermore, the pull-in voltage increase is negligible (both structures actuate with 15–20 V) because most of the electrostatic force is concentrated on the ground-plane switch pads. Finally, both structures experienced some warping along their width, but this did not prove to be a problem. The switches were thin enough that were able to conform on the dielectric surface in the down state.

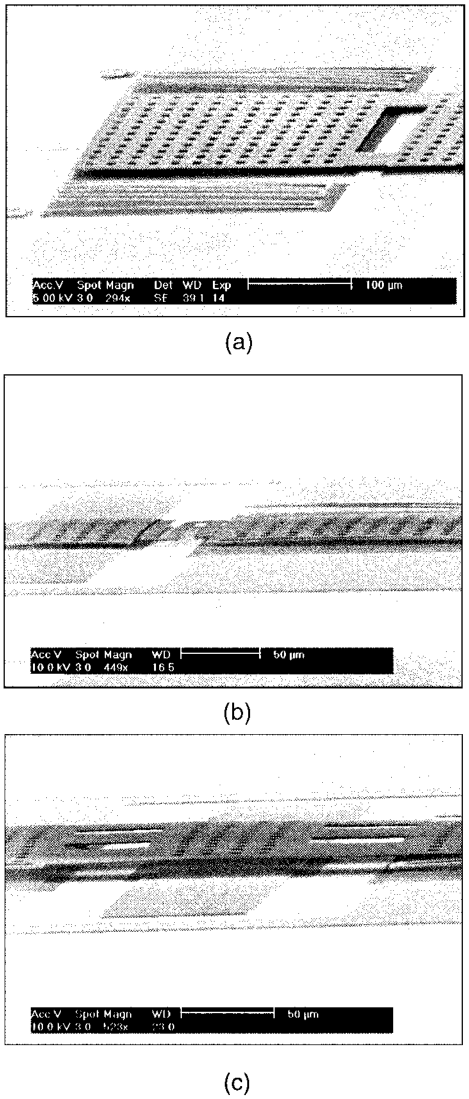

Fig. 12. Very flat switches fabricated with sputtered Ti layer instead of evaporated. (a) This three-meander switch is 640-μm long, 2-μm thick, its maximum out-of-plane deformation is less approximately 0.5 μm, and the used sacrificial layer was polyimide. (b) and (c) These switches are 680-μm long, 1-μm thick, and photoresist was their sacrificial layer. Their warping level is approximately 3 μm and is mostly along their short dimension.

B. In-Plane Residual Stress

In-plane residual stress primarily increases the switch spring constant and is, therefore, essential to control it within reasonable limits. It was experimentally found [27] that the induced tensile stress during the fabrication process was in the order of 150 MPa. A first-order approximation that shows the impact of this stress on the spring constant is analyzed in [29] where the deflection of a guided-end cantilever is calculated under simultaneous axial tension and concentrated transverse loading. The maximum deflection at the tip of the beam is given by

$$z_{\max} = \frac{W}{\gamma P}\left[\frac{\left(\cosh(\gamma l) - 1\right)^2}{\sinh(\gamma l)} - \left(\sinh(\gamma l) - \gamma l\right)\right] \qquad (12)$$

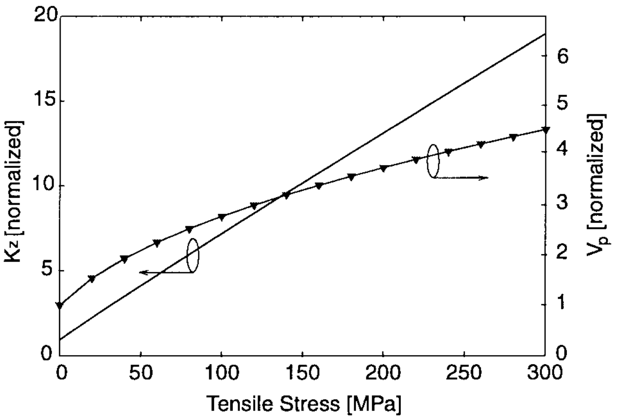

Fig. 13. Spring constant and pull-in voltage as a function of axial residual stress for a guided-end cantilever with simultaneous axial tension and concentrated transverse loading.

where P is the axial tensile load, W is the transverse concentrated load at the tip of the beam, l is the length of the beam, and γ is defined by

$$\gamma = \sqrt{\frac{P}{EI_x}}. \tag{13}$$

This leads to the following expression for the spring constant:

$$K_z^{\text{cant}} = \frac{\gamma P \sinh(\gamma l)}{2\big(1-\cosh(\gamma l)\big) + \gamma l \sinh(\gamma l)}. \tag{14}$$

Fig. 13 shows the variation of the normalized spring constant and the associated actuation voltage (with respect to the spring constant and actuation voltage of zero axial stress) for an axial tensile stress of 0–300 MPa. This figure clearly demonstrates the considerable impact of the axial stress on the switch actuation voltage. For instance, a tensile stress of 150 MPa would increase the pull-in voltage of a switch suspended by four cantilever beams by over three times.

The serpentine beams shown in Fig. 2 exhibit higher flexibility in handling the in-plane mean stress than the simple cantilever beam. In other words, as the number of meanders is increased, not only is the z-directed spring constant reduced, but also the lateral ones. To show this effect, the x- and y-directed spring constants were calculated with a similar process to that of Section II. The y-directed spring constant can be expressed as

$$k_y = \frac{\frac{2S_{1y}}{Nb^2}EI_z}{2\left(a+\frac{2b}{3}\right)S_{1y} - (a+b)S_{2y} - 3(2N+1)a(a+b)^2} \tag{15}$$

where S_{1y} and S_{2y} are calculated by

$$S_{1y} = 4N^2a^2 + \left(4N^2-1\right)b^2 + 2\left(4N^2+1\right)ab \tag{16}$$

$$S_{2y} = 2N(2N-3)a^2 + \left(4N^2-1\right)b^2 + \left(8N^2-6N-1\right)ab. \tag{17}$$

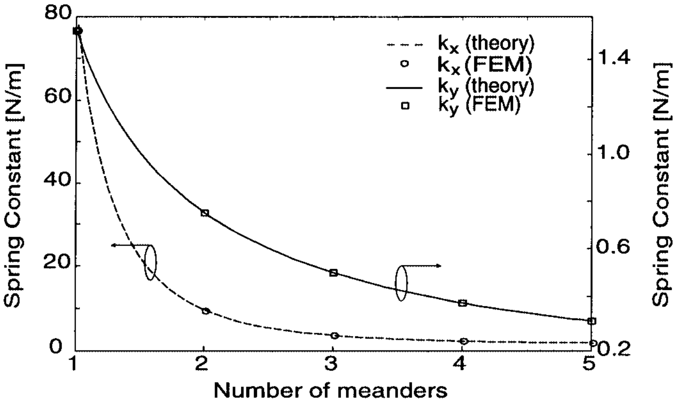

Fig. 14. In-plane spring constants of the serpentine spring for various number of meanders.

Similarly, the x-directed spring constant is given by

$$k_x = \frac{EI_z}{Na^2\left[S_{1x} + S_{2x} + \frac{8N^2a + (2N+1)(4N+1)b}{3}\right]} \tag{18}$$

where

$$S_{1x} = \big(2Na + (2N+1)b\big)\left[-\frac{2N+1}{2} + \frac{a\left(a+\frac{2b}{3}\right)}{(a+b)\left(a+\frac{b}{3}\right)}\right] \tag{19}$$

$$S_{2x} = -(2N+1)(a+b)\frac{a}{2\left(a+\frac{b}{3}\right)}. \tag{20}$$

Linear FEM simulations verified the previous formulas and the results are given in Fig. 14. From this figure, we clearly observe that the spring constant of the serpentine spring is greatly reduced as the number of meanders is increased. For instance, a spring with three meanders is 177 times more flexible along the x-dimension than a spring with one meander. As a result, such a spring can help release the axial switch stress along its long dimension much more effectively than a spring with one meander. In other words, springs with many meanders are much more effective as stress buffers than springs with one only one meander. A similar tendency exists for k_y, which decreases by a factor of 5.2 when the meanders are increased from one to five. These results provide a qualitative explanation for the trends observed in Fig. 5.

IV. MEMS SWITCH DYNAMIC BEHAVIOR

Switching speed is one of the few disadvantages of MEMS components compared to p-i-n diodes and FET transistors. While their mass is typically very small (in the order of $10^{-11}$to 10^{-9} kg), inertia due to mechanical movement still limits their speed typically in the order of a few microseconds. The fastest switch thus far has been developed by researchers at the Massachusetts Institute of Technology (MIT) Lincoln Laboratories [3]. It is a very compact cantilever switch (less than 50-μm long) with a speed of approximately 1 μs. This very low speed is primarily due to its very small dimensions, mass, and limited

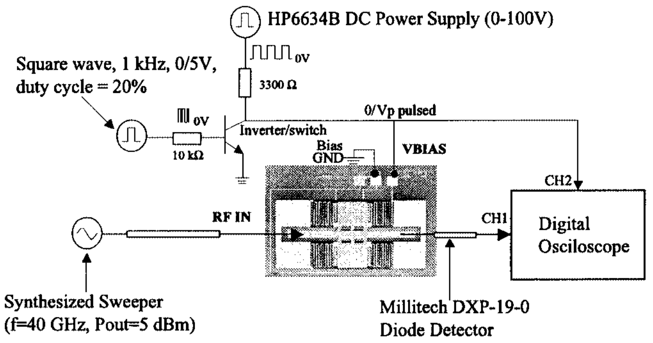

Fig. 15. Switching speed measurement setup (courtesy of Gabriel Rebeiz, The University of Michigan at Ann Arbor).

squeeze-film damping. It does require, however, a high pull-in voltage of 50–60 V, while it is typically actuated with 70–80 V. Low-voltage switches are generally expected to be slower since they typically have to move a relatively large actuation area. This is particularly true if the switch is expected to operate in air or another gas environment, such as N_2 for limiting the humidify level around the structure.

The switching speed is measured by recording the change in the power transmitted through the switch when a step voltage is applied at the bias of the device (Fig. 15) [30]. The RF input signal at 40 GHz is provided by an RF synthesizer, while the RF output signal is recorded by a high-frequency diode detector. The biasing signal is provided by a suitable combination of two dc power supplies and an inverter. Fig. 16 presents two typical measurements taken with this set-up for three-meander switches. The measured switches were suspended a mean distance of 5 μm above the CPW line and the applied bias voltage was only 20%–30% higher than their actuation voltage. Both pull-in and release times were measured for these switches. Pull-in time is the time it takes the switch to touch the dielectric underneath it. On the other hand, the time that is required for the switch to move from the down state to its original height (or within 5% from this value) is defined as the release time. Fig. 16 shows that the actuation and release times are approximately 52 and 213 μs, respectively. However, for the release time measurement, it takes the switch only 25 μs to reach its normal height, but another 190 μs are needed to settle within 5% of its original height. It is also interesting to note that, during the first 30 μs of the actuation stage, the switch does not move significantly. These effects will be discussed in the remainder of this section.

To explain the experimental results, we employed a simple one-dimensional (1-D) nonlinear model that has been adopted by several researchers [17], [31], [32]. This model treats the switch as a single lumped mass and applies classical Newtonian mechanics to predict its behavior under the applied electrostatic force. A model that would accurately predict the dynamic behavior of the MEMS structure should integrate a good understanding of several different phenomena including electrostatics, mechanics, residual stress, contact forces, compressible squeeze film damping, and impact effects on a microscale. Many of these areas are currently under investigation and there is not a complete model that would account for all of these effects. Furthermore, our switch is a relatively large structure that cannot be perfectly approximated as a lumped mass. Nevertheless, the 1-D model can be used for an at least qualitative explanation of the measured switch behavior and provide reasonable approximations for the switching times.

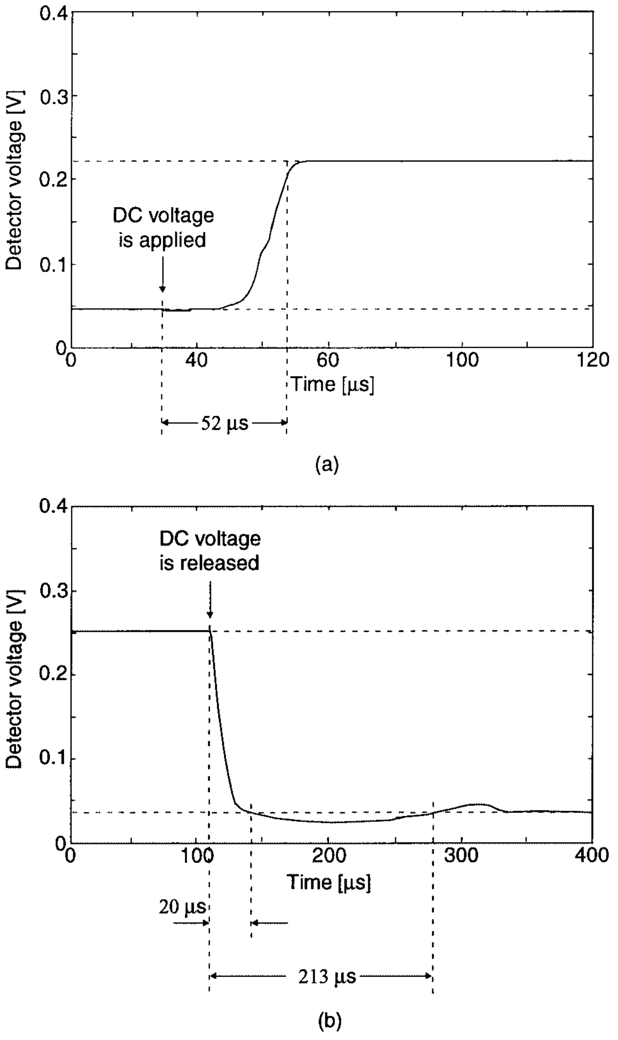

Fig. 16. Measurements of the switching time for the: (a) up–down and (b) down–up movements. Due to the diode detector, high-voltage level corresponds to low RF power and vice-versa.

The following equation of motion if the basic formula for the 1-D model:

$$mz'' + bz' + K_z z = F_e + F_c \tag{21}$$

where m is the switch mass, b is the damping coefficient, K_z is the switch spring constant in the direction of motion, A is the switch actuation area, g_0 is the initial gap, ϵ_r and t_d are the dielectric layer constant and thickness, respectively, V is the applied dc voltage, F_e is the electrostatic force, and F_c is the contact force when the switch touches the dielectric. Several approximations may be adopted for calculating the parameters in this model. For instance, although the viscous damping can be considered constant for small displacements, this is not the case when the switch is moving completely toward the substrate. Our model for the switching speed calculations is based on the discussion presented in [31] and [33] where these effects are taken into account. These equations can be summarized as follows:

$$F_e = \frac{\epsilon_0 A V^2}{2\left(g_0 + \frac{t_d}{\epsilon_r} - z\right)^2} \tag{22}$$

$$b = \frac{K_z}{\omega_0 Q}, \qquad \text{where} \quad \omega_0 = \sqrt{\frac{K_z}{m}} \tag{23}$$

$$Q = Q_0 \left(1 - \left(\frac{z}{g_0}\right)^2\right)^{3/2} \left(1 + 9.638\left(\frac{\lambda}{g_0 - z}\right)^{1.159}\right) \tag{24}$$

$$F_c = \frac{m_1 A}{(g_0 - z)^3} - \frac{m_2 A}{(g_0 - z)^{10}}. \tag{25}$$

Equation (24) calculates the switch quality factor and takes into account the damping dependence on the switch height. If this is ignored, the second term of the right-hand side should be replaced by one. Furthermore, the third term reduces the gas flow resistance underneath the switch because of the slip effect, where particles can have fewer interactions before escaping [34]. The variable λ of this term is the called the mean free path and is approximately 0.1 μm at standard temperature pressure (STP). The damping coefficient, which is related to Q_0 by (23), has been derived in [35] for a square plate with area A as

$$b = \frac{3}{2\pi}\frac{\mu A^2}{g_0^3} \tag{26}$$

where μ is the air viscosity (at STP $\mu = 1.845 \cdot 10^{-5}$ Pa $\cdot$ s). For the switch dimensions and for a gap of 5 μm $b \simeq 2.5 \cdot 10^{-4}$ Pa $\cdot$ s and $Q_0 = 0.64$ (for $K_z = 8.6$ N/m). However, the holes included in the switch allow the air underneath to escape more easily, thus reducing the damping coefficient and increasing the Q of the structure. Therefore, this value can be considered as a low bound for the switch quality factor. In fact, our experimental results suggest a quality factor of about two. The final equation of the model (25) was used to provide a stable solution to the simulation when the switch contacts the dielectric layer.

Fig. 17(a) shows the simulated results for the pull-in and release time. A spring constant of 8.6 N/m (Table II) and an actuation voltage of 25% higher than the pull-in voltage have been used for these simulations. These simulations provide a valuable insight in the measured dynamic behavior of the switch. The pull-in time, for instance, is approximately 50 μs, from which approximately 30 μs are needed for the switch to move from 5 to 3.5 μm. The RF capacitance, however, does not change appreciably between this distance and this explains the relatively long period that is required to note any difference between the measured output power level (see Fig. 16). On the other hand, during the release stage, the switch reaches its original height within 35 μs, but 140 additional microseconds are required for stabilization within 5% of its original height. We have also plotted in the same figure the simulated release time assuming a constant quality factor $Q = Q_0$. Evidently, taking into account the quality-factor variation versus height is of vital importance for meaningful simulations.

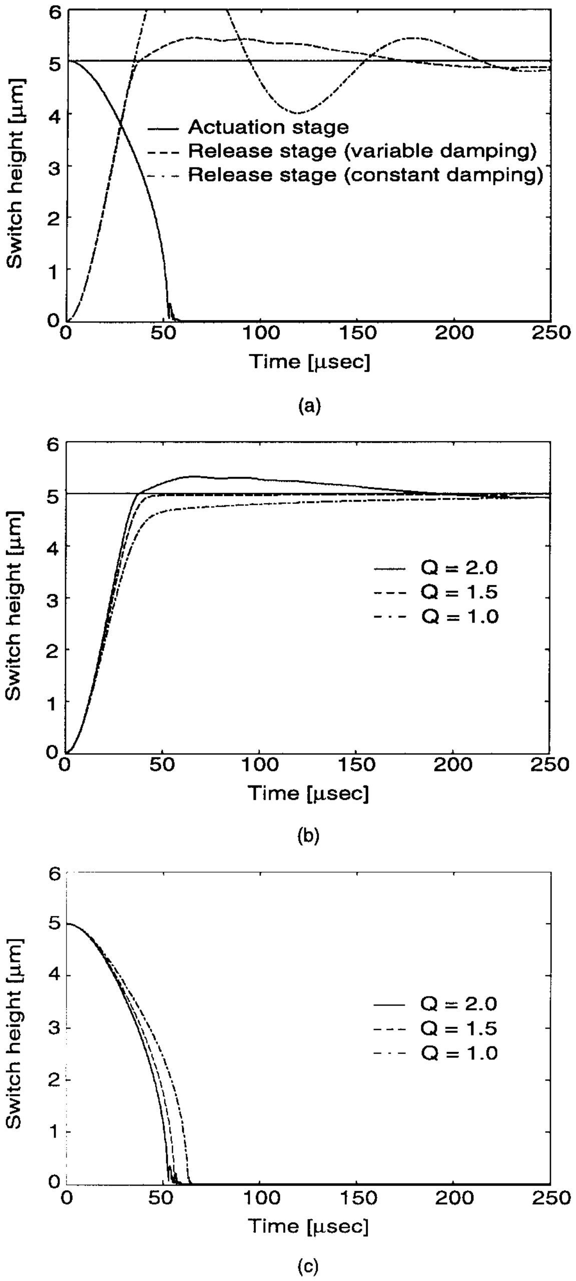

Fig. 17. (a) Simulated switch pull-in and release times. (b) Comparison of simulated release times for different values of the quality factor. (c) Comparison of simulated pull-in times for different values of the quality factor.

The problem of the long stabilization time can be easily corrected by decreasing the quality factor by approximately one. Fig. 17(b) shows the simulated release time for quality factors of 2, 1.5, and 1. This figure clearly demonstrates that the release time can be decreased by more than three times if a lower quality factor is achieved. This can be done by optimizing the hole orientation on the main switch structure and by reducing their number per unit area. This change will not appreciably increase the pull-in time, as shown in Fig. 17(c). For example, for $Q = 1.5$, the pull-in time will be increased by only 10%, yet the release time will be reduced by 300%. Consequently, an optimization of the switch holes can lead to a design with switching times in the order of 50–60 μs.

V. CONCLUSIONS

Low-voltage RF MEMS switches have been studied in this paper. The design, fabrication, and testing of these structures has been thoroughly discussed and switch designs with as low as 6-V actuation voltages have been measured. Moreover, residual stress issues associated with this family of switches have been addressed and it has been experimentally demonstrated that sputtered seed layer films result in devices with superior performance when compared with evaporated films. Furthermore, the dynamic operation of low-voltage switches has been experimentally and theoretically characterized and adequate switching speeds in the order of 50 μs have been achieved.

ACKNOWLEDGMENT

The authors are grateful to G. L. Tan, The University of Michigan at Ann Arbor, and G. M. Rebeiz, The University of Michigan at Ann Arbor, for designing and developing the measurement setup shown in Fig. 15.

REFERENCES

[1] R. E. Mihailovich, M. Kim, J. B. Hacker, E. A. Sovero, J. Studer, J. A. Higgins, and J. F. DeNatale, "MEM relay for reconfigurable RF circuits," *IEEE Microwave Wireless Comp. Lett.*, vol. 11, pp. 53–55, Feb. 2001.

[2] D. Hyman, A. Schmitz, B. Warneke, T. Y. Hsu, J. Lam, J. Brown, J. Schaffner, A. Walston, R. Y. Loo, M. Mehregany, and J. Lee, "Surface-micromachined RF MEMS switches on GaAs substrates," *Int. J. RF Microwave Computer-Aided Eng.*, vol. 9, pp. 348–361, Aug. 1999.

[3] S. Duffy, C. Bozler, S. Rabe, J. Knecht, L. Travis, P. Wyatt, C. Keast, and M. Gouker, "MEMS microswitches for reconfigurable microwave circuitry," *IEEE Microwave Wireless Comp. Lett.*, vol. 11, pp. 106–108, Mar. 2001.

[4] P. M. Zavracky, N. E. McGruer, R. H. Morrison, and D. Potter, "Microswitches and microrelays with a view toward microwave applications," *Int. J. RF Microwave Computer-Aided Eng.*, vol. 9, pp. 338–347, July 1999.

[5] C. L. Goldsmith, Z. Yao, S. Eshelman, and D. Denniston, "Performance of low-loss RF MEMS capacitive switches," *IEEE Microwave Guided Wave Lett.*, vol. 8, pp. 269–271, Aug. 1998.

[6] G. L. Tan and G. M. Rebeiz, "DC-26 GHz MEMS series-shunt absorptive switches," in *IEEE MTT-S Int. Microwave Symp. Dig.*, vol. 1, May 2001, pp. 325–328.

[7] D. Peroulis, K. Sarabandi, and L. P. B. Katehi, "Low contact resistance series MEMS switches," in *IEEE MTT-S Int. Microwave Symp. Dig.*, vol. 1, June 2002, pp. 223–226.

[8] J. B. Muldavin and G. M. Rebeiz, "High-isolation CPW MEMS shunt switches—Part 1: Modeling," *IEEE Trans. Microwave Theory Tech.*, vol. 48, pp. 1045–1052, June 2000.

[9] G. M. Rebeiz and J. B. Muldavin, "RF MEMS switches and switch circuits," *IEEE Microwave Mag.*, vol. 2, pp. 59–71, Dec. 2001.

[10] S. P. Pacheco, L. P. B. Katehi, and C. T. Nguyen, "Design of low actuation voltage RF MEMS switch," in *IEEE MTT-S Int. Microwave Symp. Dig.*, vol. 1, June 2000, pp. 165–168.

[11] D. Peroulis, S. Pacheco, K. Sarabandi, and L. P. B. Katehi, "MEMS switches for high-isolation switching and tunable filtering," in *IEEE MTT-S Int. Microwave Symp. Dig.*, vol. 2, June 2000, pp. 1217–1220.

[12] N. S. Barker and G. M. Rebeiz, "Optimization of distributed MEMS transmission-line phase shifters—U-band and W-band design," *IEEE Trans. Microwave Theory Tech.*, vol. 48, pp. 1957–1966, Nov. 2000.

[13] J. S. Hayden and G. M. Rebeiz, "Low-loss cascadable MEMS distributed X-band phase shifters," *IEEE Microwave Guided Wave Lett.*, vol. 10, pp. 142–144, Apr. 2000.

[14] D. Peroulis, S. Pacheco, K. Sarabandi, and L. P. B. Katehi, "Tunable lumped components with applications to reconfigurable MEMS filters," in *IEEE MTT-S Int. Microwave Symp. Dig.*, vol. 1, June 2001, pp. 341–344.

[15] J. C. Chiao, Y. Fu, J. M. Chio, M. DeLisio, and L. Y. Lin, "MEMS reconfigurable antenna," in *IEEE MTT-S Int. Microwave Symp. Dig.*, vol. 2, June 1999, pp. 1515–1518.

[16] C. Goldsmith, J. Ehmke, A. Malczewski, B. Pillans, S. Eshelman, Z. Yao, J. Brank, and M. Eberly, "Lifetime characterization of capacitive RF MEMS switches," in *IEEE MTT-S Int. Microwave Symp. Dig.*, vol. 1, June 2001, pp. 227–230.

[17] E. K. Chan, E. C. Kan, and R. W. Dutton, "Non-linear dynamic modeling of micromachined microwave switches," in *IEEE MTT-S Int. Microwave Symp. Dig.*, vol. 3, June 1997, pp. 1511–1514.

[18] R. K. Gupta and S. D. Senturia, "Pull-in time dynamics as a measure of absolute pressure," in *IEEE 10th Int. MEMS Workshop*, Jan. 1997, pp. 290–294.

[19] G. K. Fedder, "Simulation of microelectromechanical systems," Ph.D. dissertation, Dept. Elect. Eng. Comput. Sci., Univ. California at Berkeley, Berkeley, CA, 1994.

[20] S. P. Timoshenko and J. N. Goodier, *Theory of Elasticity*. New York: McGraw-Hill, 1970.

[21] CADRE Analytic, "CADRE light, v. 1.3," in *Finite Element Structural Analysis Software* Samammish, WA, 1999.

[22] D. Peroulis, S. P. Pacheco, K. Sarabandi, and L. P. B. Katehi, "RF MEMS switches with enhanced power handling capabilities," *IEEE Trans. Microwave Theory Tech.*, submitted for publication.

[23] M. T. A. Saif and N. C. MacDonald, "Planarity of large MEMS," *J. Microelectromech. Syst.*, vol. 5, pp. 79–97, June 1996.

[24] J. A. Thornton and D. W. Hoffman, "Stress related effects in thin films," *Thin Solid Films*, vol. 171, pp. 5–31, Apr. 1989.

[25] S. M. Hu, "Stress related problems in silicon technology," *J. Appl. Phys.*, vol. 70, pp. 53–79, Sept. 1991.

[26] W. Fang and J. A. Wickert, "Determining mean and gradient residual stresses in thin films using micromachined cantilevers," *J. Micromech. Microeng.*, vol. 6, pp. 301–309, Sept. 1996.

[27] L. Lin, A. P. Pisano, and R. T. Howe, "A micro strain gauge with mechanical amplifier," *J. Microelectromech. Syst.*, vol. 9, pp. 313–321, Dec. 1997.

[28] D. Peroulis, S. Pacheco, K. Sarabandi, and L. P. B. Katehi, "Alleviating the adverse stress effects of residual stress in RF MEMS switches," in *Proc. Eur. Microwave Conf.*, vol. 1, Sept. 2001, pp. 173–176.

[29] R. J. Roark and W. Young, *Formulas for Stress and Strain*, 6th ed. New York: McGraw-Hill, 1989.

[30] G. L. Tan, "High-performance RF MEMS circuits and phase shifters," Ph.D. dissertation, Dept. Elect. Eng. Comput. Sci., Univ. Michigan at Ann Arbor, Ann Arbor, MI, 2002.

[31] J. B. Muldavin and G. M. Rebeiz, "Nonlinear electro-mechanical modeling of MEMS switches," in *IEEE MTT-S Int. Microwave Symp. Dig.*, vol. 3, June 2001, pp. 2119–2122.

[32] F. Shi, "Dynamic analysis of micro-electro-mechanical systems," *Int. J. Numer. Methods Eng.*, vol. 39, pp. 4119–4136, 1996.

[33] J. B. Muldavin, "Design and analysis of series and shunt MEMS switches," Ph.D. dissertation, Dept. Elect. Eng. Comput. Sci., Univ. Michigan at Ann Arbor, Ann Arbor, MI, 2001.

[34] T. Veijola, H. Kuisma, J. Lahdenpera, and T. Ryhanen, "Equivalent-circuit model of the squeezed gas film in a silicon accelerometer," *Sens. Actuators A, Phys.*, vol. 48, pp. 239–248, May 1995.

[35] J. J. Blech, "On isothermal squeeze films," *J. Lubrication Tech.*, vol. 105, pp. 615–620, October 1983.

Dimitrios Peroulis (S'91–M'02) was born in Athens, Greece, in 1975. He received the Diploma degree in electrical and computer engineering from the National Technical University of Athens, Athens, Greece, in 1993, the M.S. degree in electrical engineering from The University of Michigan at Ann Arbor, in 1999, and is currently working toward the Ph.D. degree at The University of Michigan at Ann Arbor.

His current research is focused on MEMS and their applications to reconfigurable circuits and antennas for microwave and millimeter-wave frequencies.

Mr. Peroulis was the recipient of the 2002 Rackham Graduate School Pre-Doctoral Fellowship presented by The University of Michigan at Ann Arbor and the Third Place Award at the Student Paper Competition presented at the 2001 IEEE Microwave Theory and Techniques Society (IEEE MTT-S) International Microwave Symposium, Phoenix, AZ. He was also the recipient of two Student Paper Awards (honorable mentions) at the Student Paper Competitions presented at the 2002 IEEE MTT-S International Microwave Symposium, Seattle, WA, and the 2001 IEEE Antennas and Propagation Society (IEEE AP-S) International Symposium, Boston, MA, and two awards for academic excellence presented by the Technical Chamber of Greece and the Hellenic National Science Fellowship Foundation in 1997 and 1996, respectively.

Sergio P. Pacheco was born in Salvador, Bahia, Brazil, in 1969. He received the B.S.E.E. and M.S.E.E. degrees from Auburn University, Auburn, AL, in 1993 and 1995, respectively, and is currently working toward the Ph.D. in electrical engineering at The University of Michigan at Ann Arbor.

Since May 2001, he has been a Senior Staff Engineer with the Emerging Technologies Group, Digital DNA Laboratories, Motorola, Tempe, AZ. His research is focused on the application of MEMS to RF and wireless applications.

Mr. Pacheco is member of the IEEE Microwave Theory and Techniques Society (IEEE MTT-S) and the IEEE Electron Device Society (IEEE ED-S). He is also a member of the Omicron Delta Kappa, Eta Kappa Nu, and Tau Beta Pi Honor Societies. He was the recipient of the Judge's Best Paper Award presented at the IEEE MTT-S International Microwave Symposium in 1998.

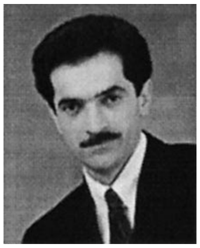

Kamal Sarabandi (S'87–M'90–SM'92–F'00) received the B.S. degree in electrical engineering from the Sharif University of Technology, Tehran, Iran, in 1980, and the M.S.E. and Ph.D. degrees from The University of Michigan at Ann Arbor, in 1986 and 1989, respectively, both in electrical engineering.

From 1980 to 1984 he was a Microwave Engineer with the Telecommunication Research Center. He is currently the Director of the Radiation Laboratory and a Professor in the Department of Electrical Engineering and Computer Science, The University of Michigan at Ann Arbor. He was the Principal Investigator of many projects sponsored by the National Aeronautics and Space Administration (NASA), Jet Propulsion Laboratory (JPL), Army Research Office (ARO), Office of Naval Research (ONR), Army Research Laboratory (ARL), National Science Foundation (NSF), Defense Advanced Research Projects Agency (DARPA), and numerous industries. He has authored or coauthored numerous book chapters and over 90 papers in refereed journals on electromagnetic scattering, random media modeling, wave propagation, antennas, microwave measurement techniques, radar calibration, inverse scattering problems, and microwave sensors. He has also had over 170 papers and invited presentations in national and international conferences and symposia on similar subjects. His research areas of interest include electromagnetic-wave propagation, antennas, and microwave and millimeter-wave radar remote sensing. He is listed in *Who's Who in American Men and Women of Science*, *Who's Who in America*, and *Who's Who in Electromagnetics*.

Dr. Sarabandi is a member of the IEEE Geoscience and Remote Sensing Society (IEEE GRSS) Administrative Committee (AdCom), chairman of the Awards Committee of the IEEE GRSS, and a member of the IEEE Technical Activities Board Awards Committee. He is also a member of Commission F, International Scientific Radio Union (URSI), and the Electromagnetic Academy. He is the associate editor of the IEEE TRANSACTIONS ON ANTENNAS AND PROPAGATION and the IEEE SENSORS JOURNAL. He was the recipient of the Henry Russel Award presented by the Regent of The University of Michigan, the GAAC Distinguished Lecturer Award presented by the German Federal Ministry of Education, Science and Technology in 1999, and the 1996 Teaching Excellence Award presented by the Electrical Engineering and Computer Science Department, The University of Michigan at Ann Arbor.

Linda P. B. Katehi (S'81–M'84–SM'89–F'95) received the B.S.E.E. degree from the National Technical University of Athens, Athens, Greece, in 1977, and the M.S.E.E. and Ph.D. degrees from the University of California at Los Angeles, in 1981 and 1984, respectively.

In September 1984, she joined the faculty of the Electrical Engineering and Computer Science Department, The University of Michigan at Ann Arbor, as an Assistant Professor, and then became an Associate Professor in 1989 and Professor in 1994. She has served in many administrative positions, including Director of Graduate Programs, College of Engineering (1995–1996), Elected Member of the College Executive Committee (1996–1998), Associate Dean For Graduate Education (1998–1999), and Associate Dean for Academic Affairs (since September 1999). She is currently the Dean of the Schools of Engineering, Purdue University, West Lafayette, IN. She has authored or coauthored 410 papers published in refereed journals and symposia proceedings and she holds four U.S. patents. She has also generated 20 Ph.D. students.

Dr. Katehi is a member of the IEEE Antennas and Propagation Society (IEEE AP-S), the IEEE Microwave Theory and Techniques Society (IEEE MTT-S), Sigma Xi, Hybrid Microelectronics, and International Scientific Radio Union (URSI) Commission D. She was a member of the IEEE AP-S Administrative Committee (AdCom) (1992–1995). She was an associate editor for the IEEE TRANSACTIONS ON MICROWAVE THEORY AND TECHNIQUES and the IEEE TRANSACTIONS ON ANTENNAS AND PROPAGATION. She was the recipient of the 1984 IEEE AP-S W. P. King (Best Paper Award for a Young Engineer), the 1985 IEEE AP-S S. A. Schelkunoff Award (Best Paper Award), the 1987 National Science Foundation Presidential Young Investigator Award, the 1987 URSI Booker Award, the 1994 Humboldt Research Award, the 1994 University of Michigan Faculty Recognition Award, the 1996 IEEE MTT-S Microwave Prize, the 1997 International Microelectronics and Packaging Society (IMAPS) Best Paper Award, and the 2000 IEEE Third Millennium Medal.